中国光学（中英文） Chinese Optics 核心期刊

石墨烯等离激元时间晶体中的慢光

何真 卓立强 李志 庄凤江 苏少坚 林志立 邱伟彬

Slow light in graphene plasmonic time crystals

HE Zhen, ZHUO Li-qiang, LI Zhi, ZHUANG Feng-jiang, SU Shao-jian, LIN Zhi-li, QIU Wei-bin

引用本文:
何真, 卓立强, 李志, 庄凤江, 苏少坚, 林志立, 邱伟彬. 石墨烯等离激元时间晶体中的慢光[J]. 中国光学, 2022, 15(4): 845-861. doi: 10.37188/CO.2021-0201
HE Zhen, ZHUO Li-qiang, LI Zhi, ZHUANG Feng-jiang, SU Shao-jian, LIN Zhi-li, QIU Wei-bin. Slow light in graphene plasmonic time crystals[J]. *Chinese Optics*, 2022, 15(4): 845-861. doi: 10.37188/CO.2021-0201

在线阅读 View online: https://doi.org/10.37188/CO.2021-0201

文章编号 2095-1531(2022)04-0845-17

Slow light in graphene plasmonic time crystals

HE Zhen, ZHUO Li-qiang, LI Zhi, ZHUANG Feng-jiang, SU Shao-jian, LIN Zhi-li, QIU Wei-bin*
(*College of Information Science and Engineering*, *Huaqiao University*, *Xiamen* 361021, *China*)
* *Corresponding author*, *E-mail*: *wbqiu@hqu.edu.cn*

Abstract: In order to control the group velocity of slow light, a graphene plasmon time crystal slow light waveguide was constructed and used for the waveguide to construct the Zigzag topology interface channel for transmission. When the structure is fixed, the external bias voltage of the graphene nano-disk can be dynamically adjusted to obtain the dispersion curves at different times. The corresponding group velocity is studied. First, the graphene plasmon time crystal is obtained by applying the bias voltages periodically varying with time to different regions of the honeycomb arranged graphene nano-disks. When the time translation symmetry of the crystal is destroyed, the crystal band gap will periodically appear and disappear with time, and exhibit the band topology effect. The Zigzag topology interface is constructed to analyze the topological interface state and its slow light mode existing at different moments. Then the corresponding group velocity is calculated according to the dispersion curve. Finally, a slow light waveguide model is established through numerical simulation, and the field enhancement process is detected at the light energy capture point of the waveguide. Simulation results show that the waveguide designed based on the graphene plasmon time crystal can achieve a good slow light transmission effect, and the group velocity of the light can be dynamically adjusted when the waveguide structure is fixed. Under slow light transmission, the light energy capture point realizes the field enhancement effect. The slow light waveguide with simple structure can be dynamically tuned, and has broad application prospects in slow light modulation devices and optical storage devices.
Key words: slow light; graphene; plasmonic time crystal; dynamical tuning

石墨烯等离激元时间晶体中的慢光

何 真, 卓立强, 李 志, 庄凤江, 苏少坚, 林志立, 邱伟彬*
(华侨大学 信息科学与工程学院, 福建 厦门 361021)

摘要: 为了实现对慢光群速度的控制, 构建了石墨烯等离激元时间晶体慢光波导。对波导采用石墨烯等离激元时间晶体来构造用于传输的 Zigzag 拓扑界面通道, 当结构一定时动态调节石墨烯纳米盘的外加偏置电压, 即可获得若干不同时刻的色散曲线, 并对相应的群速度进行研究。首先, 通过对蜂窝状排列的石墨烯纳米盘的不同区域施加随时间周期性变化的偏置电压, 来获得石墨烯等离激元时间晶体。当晶体时间平移对称性遭到破坏时, 晶体带隙会随着时间周期性出现及

收稿日期: 2021-11-18; **修订日期:** 2021-12-16
基金项目: 国家自然科学基金资助项目(No. 11774103)
Supported by National Natural Science Foundation of China (No. 11774103)

消失，进而呈现出能带拓扑效应。接着，构造 Zigzag 拓扑界面分析不同时刻下存在的拓扑界面态及其慢光模式。然后，根据该色散曲线计算出对应的群速度。最后，通过数值仿真建立慢光波导模型，并在波导光能捕获点检测场增强过程。模拟结果表明：基于石墨烯等离激元时间晶体所设计的波导可以实现很好的慢光传输效果，在波导结构固定时可以动态调节光的群速度。慢光传输下光能捕获点实现了场增强效应。该慢光波导结构简单，可动态调谐，在慢光调制器件和光储存器件中具有广阔的应用前景。

关　键　词：慢光；石墨烯；等离激元时间晶体；动态调谐

中图分类号：TP394.1;TH691.9　　**文献标志码：**A　　**doi:** 10.37188/CO.2021-0201

1 Introduction

The slow light technology has attracted more and more attention due to its quite broad potential application prospect in optical field regulation and optical storage devices[1-3]. Controlling the structure dispersion to realize slow light is one of the commonly used technologies at present. The main method of this technology is to control the light group velocity by designing a slow optical waveguide with a specific structure. Slow light generated in such photonic crystal waveguides has been observed in several studies[4-5]. However, in the previous slow optical waveguide structure, when the group velocity becomes slow, its supported bandwidth is very narrow, and it is also accompanied by a huge group velocity dispersion effect. Scheuer J. *et al*. used a complex coupled resonant optical waveguide to achieve internal dispersion compensation and solved the problem of distortion[6]. In recent years, Surface Plasmon Polaritons (SPPs) waveguides have been used to realize slow light, which can achieve higher slow light capacity with a fixed structure, but the adjustment of slow light performance is limited[7]. In addition, the large group velocity dispersion effect of the chirped structure can cause seriously distortion of the optical signal, and the device has a limited operating frequency range[8]. Furthermore, the structural design of traditional slow-light devices is complicated and their tunability is poor once the structure is fixed, which limits their practical applications.

Photonic crystals have good topological band effects, and their topological concepts have great potential in the application of photonics, which has attracted extensive attention. Topological photonic structures have subverted some conventional views on wave propagation and manipulation. Applying topological photonic crystals to wave propagation makes it possible to realize new photonic devices with specific funtions, such as sharp bending waves without reflection, robust delay lines, spin polarization switches and non-reciprocal devices[9]. Recently, Chen Xiaodong *et al*. proposed and proved that the valley states in topological photonic crystals can be used as topological protection to realize light transmission. The design is to place two topological photonic crystals with different topological structures in mirror images to form an interface that can achieve topological protection[10]. Later, Yoshimi *et al*. proposed a method to realize topological slow optical waveguides in valley photonic crystals[11]. The waveguide structure is based on a semiconductor substrate to realize slow light transmission with a group index greater than 100 in the topological band gap range, but the manufacturing process is complex, and the structure has no tunability and does not involve the change of field strength caused by slow light. With the deepening of research, it is found that the topological band gap structure of valley state can be realized in photonic time crystal materials whose refractive index changes periodically with time[12]. The method is that by breaking the crystal time translation symmetry, photonic time crystals can achieve topologically non-trivial phases[13-15], thereby affecting the propagation of light in the crystal.

It is well known that graphene has unique electrical and optical properties, especially it supports

surface plasmonic excitation waves, and has relatively low ohmic loss and high tunability[16]. Jin *et al*. designed monolayer graphene with periodic patterns to achieve topological unidirectional boundary transport by introducing a static magnetic field[17]. Later, Wang Yang *et al*. realized topological valley plasmonic transport in bilayer graphene metasurfaces for sensing applications[18]. Recently, Guo Xiang *et al*. designed a graphene SPP equivalent two-dimensional photonic crystal slow light waveguide through photonic crystal line defects, and achieved slow light modulation through the gradual change of chemical potential of graphene in space[19]. Likewise, it is very important to realize the modulation of the slow light transport in the valley state topology of graphene plasmonic crystals in time. In this paper, we propose a novel approach to achieve topological slow light transport in waveguides constructed from graphene plasmonic time crystals. Two-dimensional graphene plasmonic time crystals consist of a set of graphene nanodisks periodically arranged in a honeycomb pattern. By controlling the periodic change of the chemical potential of graphene with time, the time-translational symmetry of graphene plasmonic time crystals is broken. Numerical simulations show that the plasmonic time crystal band gap can open and close periodically with time. Further, we find that the Zigzag edges can support near-zero electromagnetic transport group velocities within the topological bandgap. Numerical simulation results of electromagnetic transmission in slow light waveguide show that the topological waveguide can generate slow light. The advantages of this method are simple structure, good field enhancement effect and dynamic tuning ability, which provides a new way for dynamically realizing optical field regulation.

2 Numerical simulation methods and models

In this paper, a valley state topological slow optical transmission waveguide is implemented based on graphene plasmonic time crystals. As shown in Fig. 1(a) (Color online), the waveguide adopts the Zigzag structure topological interface as the transmission channel, and the top is composed of graphene nanodisks. Graphene is in contact with air, SiO_2 is selected as the background material, and Si as the substrate material. It can be seen from the

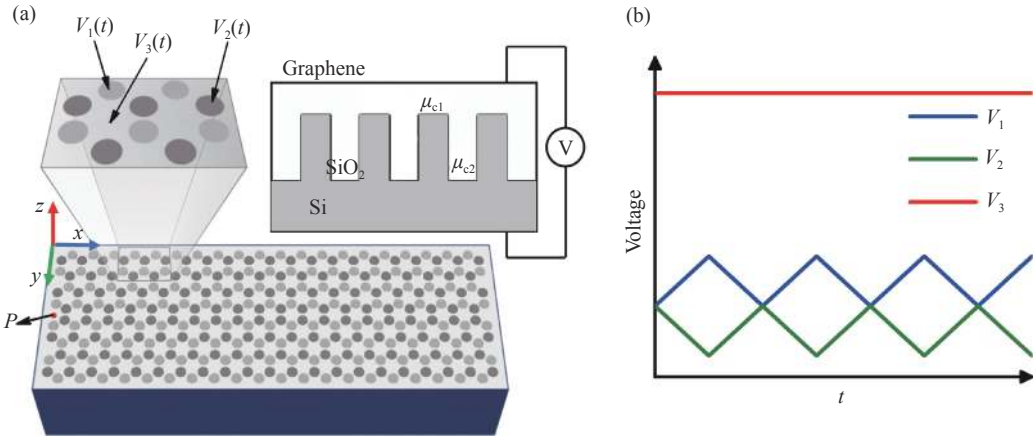

Fig. 1 (a) The three-dimensional schematic of slow light waveguide, with a single layer of graphene nanodisks at the top. The graphene is exposed to air on the top, the background material is SiO_2, and the substrate material is Si. Different graphene nanodisks are applied with different bias voltages: $V_1(t)$, $V_2(t)$ and $V_3(t)$. The diagram on the right shows how voltage is applied. (b) The graphene nanodisk's external bias voltage changes periodically with time

图 1 (a) 慢光波导的三维示意图, 顶部是单层石墨烯纳米盘。石墨烯与空气接触, 背景材料是 SiO_2, 衬底材料是 Si。对不同的石墨烯纳米圆盘分别加载不同的偏置电压: $V_1(t)$, $V_2(t)$ 和 $V_3(t)$, 右上图为电压的施加方式。(b) 石墨烯纳米盘外加偏置电压随时间周期性变化的曲线

cross-sectional view of the waveguide in the figure that the bias voltage is applied to the graphene nanodisk and the silicon substrate. The silicon pillars are arranged in a triangular lattice, and $V_1(t)$, $V_2(t)$ and $V_3(t)$ are the bias voltages applied to the graphene nanodisks, respectively. This method is based on the photonic crystal realization mechanism of the graphene plasmonic exciton[20]. When the distance between graphene and the substrate is constant, the chemical potential of graphene can be changed by changing the applied voltage.

It is assumed that the relative permittivity of the surrounding environment of graphene is ε_{r1} and ε_{r2}, respectively. The relative permittivity of the substrate SiO_2 is ε_{r1}=3.9, and the relative permittivity of the air on the upper surface of the graphene is ε_{r2}=1. In our numerical simulation, the TM mode is considered and the electric field form of TM mode is assumed to be[21]:

$$\begin{cases} E_x = A\mathrm{e}^{\mathrm{i}\beta x - Q_1 z},\ E_y = 0, E_z = B\mathrm{e}^{\mathrm{i}qx - Q_1 x},\ (z>0) \\ E_x = A\mathrm{e}^{\mathrm{i}\beta x + Q_2 z},\ E_y = 0, E_z = B\mathrm{e}^{\mathrm{i}qx + Q_2 x},\ (z<0) \end{cases} . \tag{1}$$

Substituting equation (1) into Maxwell's equations, adding the surface conductivity of graphene (σ_g) to participate in the formula transformation, and matching the corresponding boundary conditions, the dispersion relation of the TM mode is obtained as[22]:

$$\frac{\varepsilon_{r1}}{\sqrt{\beta^2 - \frac{\varepsilon_{r1}\omega^2}{c^2}}} + \frac{\varepsilon_{r2}}{\sqrt{\beta^2 - \frac{\varepsilon_{r2}\omega^2}{c^2}}} = -\frac{\sigma_g i}{\omega\varepsilon_0} , \tag{2}$$

where ε_0 is the vacuum permittivity in free space, ω is the angular frequency of the plasmon, and c is the propagation speed of light in vacuum. In the whole calculation process, we only consider the case of the propagation constant $\beta \ll \frac{\omega}{c}$, so equation (2) can be simplified to the following form[23]:

$$\beta = \varepsilon_0\left(\frac{\varepsilon_{r1}+\varepsilon_{r2}}{2}\right)\frac{2\omega i}{\sigma_g} , \tag{3}$$

where β is the propagation constant based on graphene SPP, the surface conductivity of graphene σ_g can be adjusted with temperature T, chemical potential μ_c, scattering rate τ and angular frequency ω, which consists of two parts: intra-band electron scattering σ_{intra} and inter-band electron transition σ_{inter}, according to Kubo Formula[23]:

$$\sigma_g = \sigma_{intra} + \sigma_{inter} , \tag{4}$$

$$\sigma_{intra} = -\mathrm{j}\frac{\mathrm{e}^2 \mathrm{k}_B T}{\pi\hbar^2(\omega - \mathrm{j}\tau^{-1})}\left[\frac{\mu_c}{\mathrm{k}_B T} + 2\ln(\mathrm{e}^{-\mu_c/\mathrm{k}_B T}+1)\right] , \tag{5}$$

$$\sigma_{inter} = \frac{-\mathrm{j}\mathrm{e}^2}{4\pi\hbar}\ln\left(\frac{2|\mu_c| - (\omega - \mathrm{j}\tau^{-1})\hbar}{2|\mu_c| + (\omega - \mathrm{j}\tau^{-1})\hbar}\right) , \tag{6}$$

where k_B is the Boltzmann constant, e is the charge of the electron, and $\hbar$ is the reduced Planck constant. Specifically, the chemical potential of graphene μ_c can be effectively tuned by an externally applied voltage[20-21, 24-25].

$$\mu_c(t) = \hbar v_F \sqrt{\frac{\pi C_{ox} V_g(t)}{\mathrm{e}}} , \tag{7}$$

where v_F is the Fermi velocity, C_{ox} is the gate capacitance[26], and $V_g(t)$ is the applied voltage that changes periodically with time. In this paper, the curve of the applied bias voltage of graphene nanodisk changing periodically with time is shown in Fig. 1(b) (Color online). By changing the bias voltages $V_1(t)$, $V_2(t)$ and $V_3(t)$ applied to the graphene nanodisks, the graphene chemical potentials $\mu_{c1}(t)$, $\mu_{c2}(t)$ and $\mu_{c3}(t)$ are changed.

3 Numerical simulation results and discussion

3.1 Graphene plasmonic time crystal model and properties

First, we explored the energy band topology of 2D graphene plasmonic crystals composed of graphene nanodisk arrays arranged in a triangular lattice. The time crystal structure of graphene plasmon is shown in Figure 2 (a). The dotted line area is the crystal cell, and the solid line part is the Brillouin region of the crystal, where $\Gamma - M - K - \Gamma$ is the reduced wedge of Brillouin region, a is the crys-

tal lattice constant, a=40 mm, and the radius of graphene nanodisk is expressed as r and r=0.21a. μ_{c1}, μ_{c2} and μ_{c3} are the chemical potentials of different graphene nanodiscs, respectively. From equation (7), it can be seen that the chemical potentials of these graphene nanodiscs can also change periodically with time, which can be written as $\mu_{c1}(t)$, $\mu_{c2}(t)$ and $\mu_{c3}(t)$[27-29]. The chemical potential of graphene nanodisks can be flexibly controlled in time by applying periodic changed bias voltage of $V_1(t)$, $V_2(t)$ and $V_3(t)$. Here, we calculate the energy bands of graphene plasmonic time crystals at several moments in one cycle, as shown in Fig. 2(b) (Color online), where the black line depicts that, when t=0 s (i.e. $\Delta\mu_c=\mu_{c1}-\mu_{c2}$=0 eV), the chemical potentials of the graphene nanodisk are $\mu_{c1}=\mu_{c2}$= 0.3 eV and μ_{c3}=0.6 eV, respectively, the two energy bands degenerate at the K point and intersect at the Dirac point, and there is obviously no band gap. During the periodic change of chemical potential with time, the time-translation symmetry of the graphene plasmonic time crystal is broken, the Dirac cone dispersion will be split, and the band gap will be opened[30]. The green, blue and red curves in Fig. 2(b) depict the band structures of the following three time nodes: t_1=1 e^{-12}s (i.e. $\Delta\mu_c$=0.1 eV), t_2=1.5 e^{-12}s (i.e. $\Delta\mu_c$=0.12 eV) and t_3= 2 e^{-12}s (i.e. $\Delta\mu_c$=0.14 eV), respectively. It is clear that the crystal band gap undergoes a process from closing to opening over time. It is worth noting here that this graphene plasmonic time crystal energy band change over time can be performed without changing the geometry.

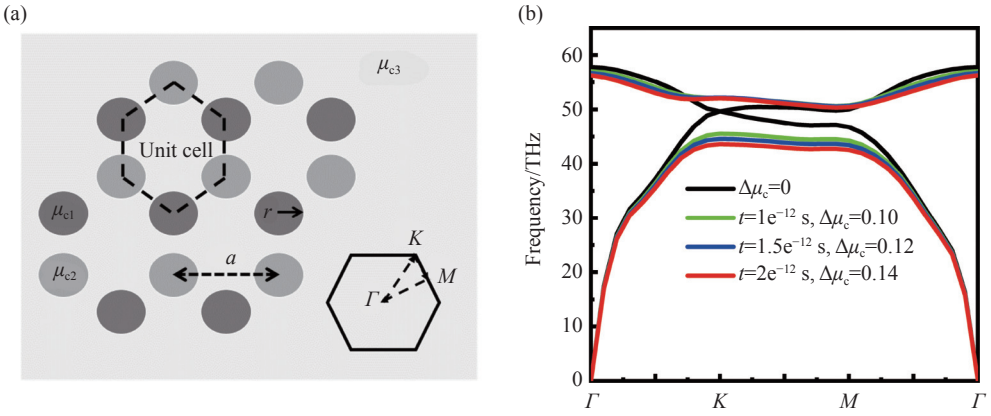

Fig. 2　(a) Schematic diagram of graphene plasmon time crystal structure. (b) Energy band diagrams of graphene plasmon time crystals at four different moments in a cycle of external bias voltage change

图 2　(a) 石墨烯等离激元时间晶体结构示意图。(b) 在一个外加偏置电压变化周期内, 石墨烯等离激元时间晶体在 4 个不同时刻的能带图

In order to verify the properties of graphene plasmonic time crystals, a numerical simulation study is designed in this work. As shown in Fig. 3(d), in a region composed of graphene plasmonic time crystals, an excitation source is placed at point P, and the relationship between the chemical potentials of graphene nanodisks satisfies the variation law shown in Fig. 3 (a). Here, electromagnetic waves with a frequency of 46.50 THz are excited from the excitation source. We further explored the change trend of crystal energy band gap with the change of graphene chemical potential. By analyzing the opening and closing of the band gap, the propagation phenomenon occurs when the frequency of the excitation wave is in the conduction band; however, when the frequency is in the band gap, the wave will not propagate in this time interval[31-33]. The simulation results are shown in Figure 3 (Color online), in which screenshots are taken of the electric fields at four time nodes during the trans-

mission process. With the periodic change of $\Delta\mu_c$ in time, the transmission and inhibition alternate phenomenon occurs in the timing of t_b=3.20 e^{-12}s, t_c=4.16 e^{-12}s, t_d= 5.82 e^{-12}s and t_f=8.24 e^{-12}s, respectively. This result can well illustrate that the graphene plasmonic time crystal can realize the periodic opening and closing of the energy band gap with time by periodically adjusting the chemical potential.

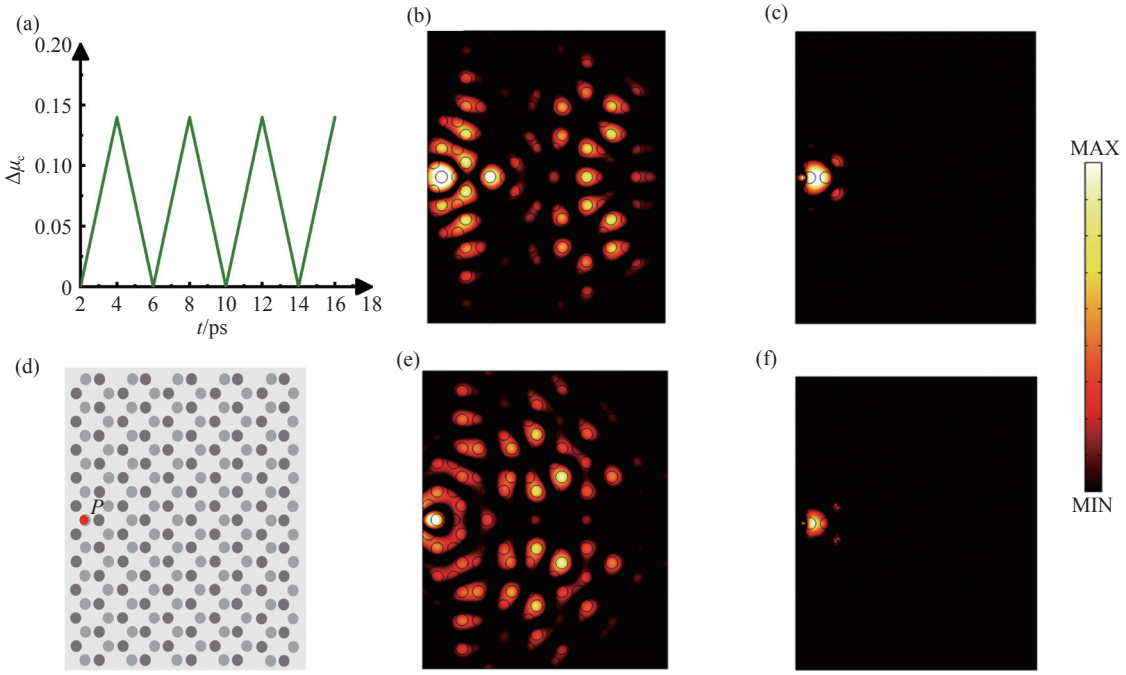

Fig. 3 (a) When μ_{c3}=0.6 eV, the relationship between $\Delta\mu_c$ and t. (d) A region composed of 5×10 graphene plasmon time crystals. P is the position of the excitation source. (b), (c), (e) and (f) Screenshots of four moments in the propagation process at the time nodes of t_b=3.20 e^{-12}s, t_c=4.16 e^{-12}s, t_d=5.82 e^{-12}s and t_f=8.24 e^{-12}s, respectively

图 3 (a) 当μ_{c3}=0.6 eV 时，$\Delta\mu_c$与 t 的关系。(d) 5×10 石墨烯等离激元时间晶体组成的一个区域，P 是激发源的位置。(b), (c), (e) 和 (f) 是传播过程中 4 个时刻的截图，时间节点分别是t_b=3.20 e^{-12}s, t_c=4.16 e^{-12}s, t_d=5.82 e^{-12}s 和t_f=8.24 e^{-12}s

3.2 Zigzag topological boundary structure theory and model

When the time-translational symmetry of the graphene plasmonic time crystal is broken, the Dirac cone dispersion is not preserved. From the point of view of group theory, when the inversion symmetry is broken, the group symmetry of the point (K or K') will be reduced from C_{3v} to C_3. In the energy band, the Dirac cone is destroyed, and the two energy bands originally degenerated to the point K will be opened[34-35]. By analyzing the change of the orbital angular momentum at the valley of the energy band after the energy band is opened, we obtain the phase distribution at point K at time of t_1=1 e^{-12}s (i.e. $\Delta\mu_c$=0.1 eV), t_2=1.5 e^{-12}s (i.e. $\Delta\mu_c$=0.12 eV) and t_3= 2 e^{-12}s (i.e. $\Delta\mu_c$=0.14 eV). As shown in Figure 4 (Color online), it can be seen that, at different times, the two energy bands appear the phase distribution of Left-handed Circular Polarization (LCP) and Right-handed Circular Polarization (RCP) at the degenerate point K, respectively, that is, in the process of $\Delta\mu_c$ changing with time, the energy valley at any moment has the circularly polarized orbital angular momentum in the opposite direction after the time crystal energy band is opened. Therefore, we construct electromagnetic transport at the topological edge through electromagnetic modes that can be loaded with different orbital angular momentums, which provides a theoretical basis for the use of topological boundary to construct slow light waveguides.

In this study, Zigzag topological boundaries are

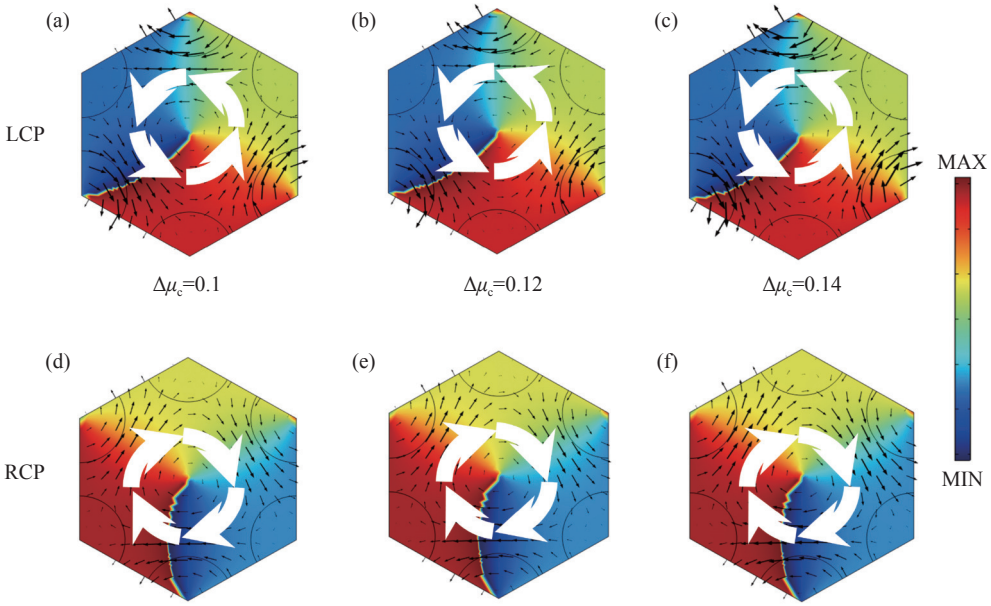

Fig. 4　The phase distributions of Left-handed Circularly Polarized (LCP) and Right-handed Circularly Polarized (RCP) of the time crystal appear at point *K*, which are expressed as the component of the electric field in the direction *Z* and the in-plane Poynting vector (P_x, P_y). (a) and (d) the phase distribution diagram of point *K* at the time of $\Delta\mu_c$=0.1 eV; (b) and (e) the phase distribution diagram of point *K* at the time of $\Delta\mu_c$=0.12 eV; (c) and (f) the phase distribution diagram of point *K* at the time $\Delta\mu_c$=0.14 eV

图 4　时间晶体在 *K* 点分别出现了左旋圆极化 (LCP) 和右旋圆极化 (RCP) 的相位分布，表示为电场在 *Z* 方向上的分量和面内坡印亭矢量 (P_x, P_y)。(a) 和 (d) 是在$\Delta\mu_c$=0.1 eV 时刻，*K* 点的相位分布图；(b) 和 (e) 是在$\Delta\mu_c$=0.12 eV 时刻，*K* 点的相位分布图；(c) 和 (f) 在$\Delta\mu_c$=0.14 eV 时刻，*K* 点的相位分布图

used to construct slow light waveguides. This topology is constructed from graphene plasmonic time crystals, which generate “ temporal topological boundary states”, they are temporal analogs of topological edge states[13]. Breaking the time-translational symmetry of graphene plasmonic time crystals will lead to the opening of Dirac points at band degeneracy, thus forming a full band gap in which topologically protected boundary modes exist. The red dotted line in Figure 5(a) (Color online) is the Zig-

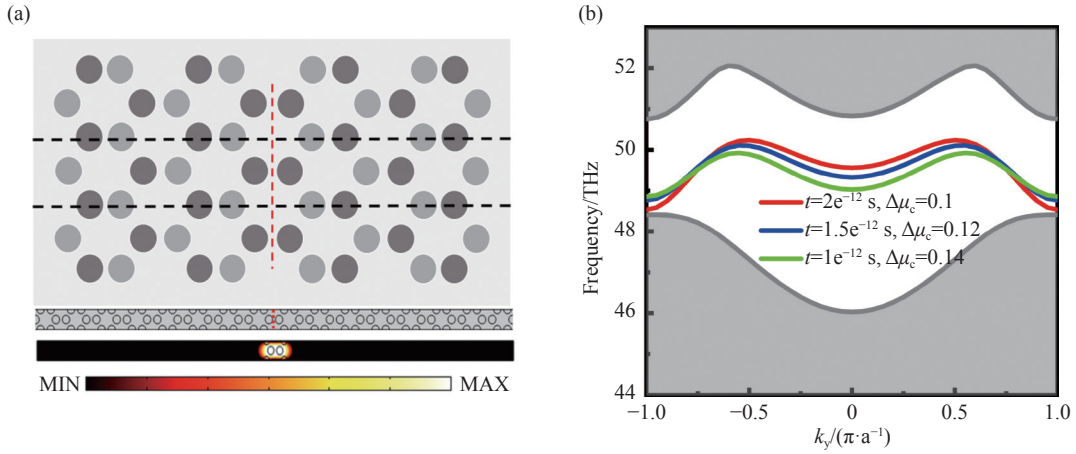

Fig. 5　(a) Schematic diagram of the Zigzag interface based on graphene plasmon time crystals, in which the bottom is the calculation model of the finite period super cell unit and the simulation electric field distribution results. (b) The dispersion curves of the Zigzag interface mode at different times

图 5　(a) 基于石墨烯等离激元时间晶体构成的 Zigzag 边界示意图。其中，底部分别是有限周期超胞单元的计算模型和仿真电场分布结果。(b) 不同时刻下 Zigzag 边界模的色散曲线

zag topology interface. By sampling the area within the black dotted line, a finite period (N=19) supercell model is established in the commercial simulation software COMSOL Multiphysics. Part of the simulation results are shown at the bottom of Fig. 5(a) (Color online), and it can be seen that the electric field distribution is concentrated at the boundary. We also calculated the dispersion relation of this boundary mode at different times (Fig. 5(b)), and the gray area represents the projected body energy band diagram. Fig. 5(b) also depicts the projected energy bands of three boundary states at the time t_1=1 e^{-12}s, t_2=1.5 e^{-12}s and t_3=2 e^{-12}s[36]. Obviously, when $\Delta\mu_c$ changes with time, there is always a corresponding boundary state at each moment, which means that the time simulation based on the Zigzag topology boundary state of the graphene plasmon time crystal is realized.

3.3 Slow light phenomenon and field enhancement effects

By further analyzing the dispersion relation of the above boundary modes, we can deduce a phenomenon that the group velocity is zero (slow light) at the extreme point of the dispersion curve. In order to better study the group velocity of guided modes existing in this boundary state, the partial dispersion curves at three different times are plotted in Fig. 6(a) (Color online). It is obvious that the dispersion is accompanied by severe bending, which leads to the existence of slow light mode in the gap. Based on the dispersion curves of these boundary modes, the change curve of the group velocity with angular frequency w can be calculated with the relationship $v_g = d\omega/dk$[37-38]. As shown in Figure 6(b) (Color online), the red curve is the group velocity at t_1=1 e^{-12}s and $\Delta\mu_c$=0.1 eV, the group velocity tends to zero, and the frequency to 50.237 0 THz. At t_2=1.5 e^{-12}s and $\Delta\mu_c$=0.12 eV, the electromagnetic wave group velocity is close to zero at the frequency of 50.114 9 THz, which is depicted in Fig. 6(b) by the blue curve. At t_3=2 e^{-12}s and $\Delta\mu_c$=0.14 eV, the group velocity is close to zero at a frequency of 49.929 2 THz, which is marked by the green curve. Numerical calculation results show that the group velocity of electromagnetic waves with different frequencies reach zero at different moments, that is, the topological boundary can realize slow light that its certain frequency electromagnetic wave group velocity near zero at different moments.

Finally, with the slow light waveguide model given in Fig. 1(a), a two-dimensional modeling is carried out in the simulation software COMSOL, the

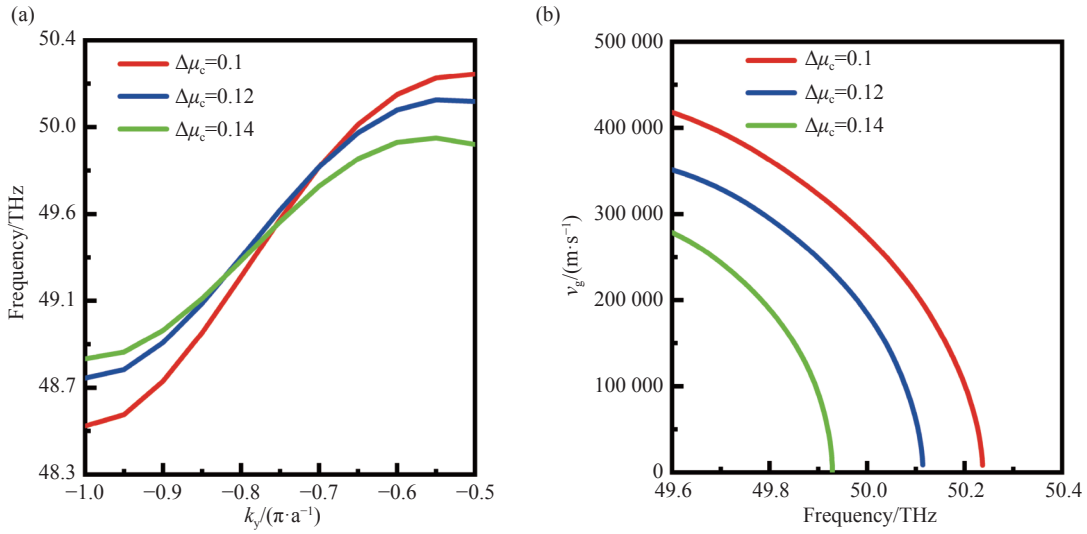

Fig. 6 (a) The boundary mode dispersion curve supported by the topological boundary under different $\Delta\mu_c$. (b) The relationship between group velocity and frequency under different $\Delta\mu_c$

图 6 (a) 不同$\Delta\mu_c$下拓扑边界所支持的边界模色散曲线。(b) 不同$\Delta\mu_c$下群速度随频率的变化关系图

Zigzag boundary structure is used as the transmission channel, and the excitation source is located at *P* (as shown in Fig. 1(a)). The chemical potential of graphene nanodisks can be flexibly controlled in time by applying a bias voltage that varies periodically with $V_1(t)$, $V_2(t)$, and $V_3(t)$. The graphene SPP wave with a certain frequency is emitted from point *P*, and the whole process of its transmission in the waveguide over time can be obtained. Figure 7 (Color online) shows the electric field intensity distribution results of plane waves with frequencies of 50.237 0 THz, 50.114 7 THz and 49.929 2 THz propagating in the waveguide respectively. In this simulation, the plane wave with a frequency of 50.237 0 THz is continuously excited from point *P* at t_0=0 s , and reaches a state where the group velocity is close to zero after traveling along the waveguide for time 1 e^{-12}s, and the SPP wave transmission stagnates at the position of *X*=307.998 nm. Figure 7(a) shows the electric field screenshot of a plane wave with a frequency of 50.237 0 THz at time t_1=1 e^{-12}s during the transmission process. After the plane wave group velocity is close to zero, the excitation in the slow light mode is continued, and it is found that the electric field intensity at the position of *X*=307.998 nm (the green dot in Fig. 7(a)) reaches the maximum value at *t*=1.4 e^{-12}s, and the electric field intensity at this time is much greater than that at the excitation source. Plotting the electric field intensity in the waveguide at *t*=1.4 e^{-12}s in Fig. 7 (b), it can be found that the field intensity *B* at the light energy capture point is greater than the field intensity *A* at the excitation source. By plotting the change process of the electric field intensity at the green dot position in the time period from t_0= 0 s to *t*=1.4 e^{-12}s is depicted in Fig. 7(c), we can see that the waveguide achieves a continuous superposition of the electric field strength at the light energy trapping point (green dot) and is higher than the enhancement effect of the excitation source due to the field enhancement effect in slow light transmission[4]. Figure 7(d) shows the electric field distribution of the SPP wave with a frequency of 50.114 7 THz from point *P*, which is continuously excited from time t_0=0 s, and propagates along the waveguide for time 1.5 e^{-12}s. When SPPs wave is transmitted to t_2=1.5 e^{-12}s, the group velocity at *X*=667.879 nm decreases to zero. In addition, we also continuously observed the electric field at the light energy capture point *X*=667.879 nm (blue dot in Fig. 7 (d)), and obtained the cross-section of the electric field distribution at the boundary at *t*= 2.98 e^{-12}s, as shown in Fig. 7 (e). This result shows that at time *t*=2.98 e^{-12}s, the electric field intensity at the light energy capture point reaches the maximum *D* and is greater than the electric field intensity *C* at point *P*. Figure 7(f) depicts the superposition process of the electric field strength at the blue dot from time t_0=0 s to *t*=2.98 e^{-12}s. Similarly, as shown in Fig. 7(g), the SPP wave with a frequency of 49.929 2 THz is continuously excited from point *P* at time t_0=0 s, and reaches a near-zero group velocity after traveling along the waveguide for 2 e^{-12}s. The light energy trapping is located at *X*=1 029.122 nm (red dot in Fig. 7(g)). Continuous excitation is carried out in the slow light mode, and it is observed that the electric field at the light energy capture place reaches the maximum intensity *F* at time *t*=3.22 e^{-12}s, which is much greater than the electric field intensity *E* at the excitation source, as shown in Figure 7(j). During the time period from t_0=0 s to *t*=3.22 e^{-12}s, the change process of the electric field intensity at the position of the red dot is depicted in Fig. 7(j), which also experienced a process of superposition of the electric field intensity. The above simulation process takes SPP waves with three different frequencies, and modulates the light group velocity close to zero by changing the applied bias voltage on the graphene nanodisk respectively. It can be seen that under the influence of the field enhancement effect, the waveguide realizes the continuous superposition of electric field intensity at the

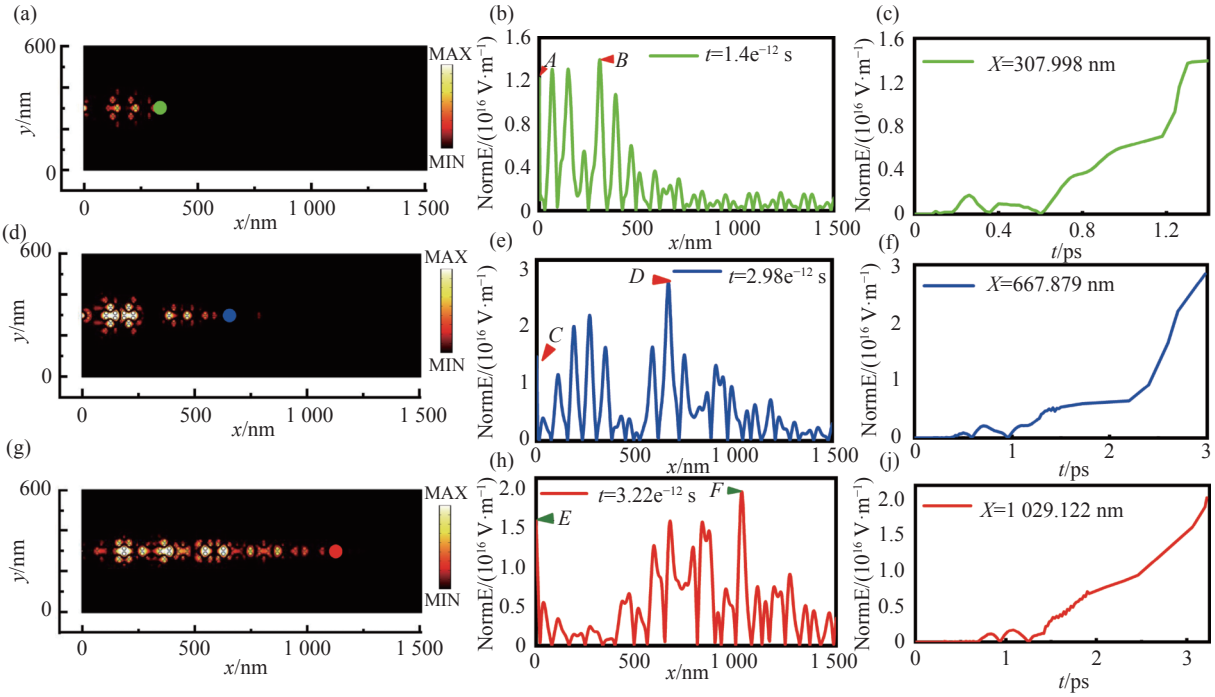

Fig. 7 (a, d, g) Screenshots of the electric field intensity distribution at t_1, t_2 and t_3. (b, e, h) Cross-sectional electric field diagrams at the Zigzag boundary at different time t. (c, f, j) The changing process of the electric field at the capture point of light energy

图 7 (a, d, g) t_1, t_2 和 t_3 时刻电场强度分布截图。(b, e, h) 不同 t 时刻 Zigzag 边界处截面电场图。(c, f, j) 光能捕获点处电场变化过程

light energy capture point, which is higher than that at the excitation source. These results show that the slow light waveguide can make the SPP waves with different frequencies stop at different times and positions, and the field enhancement effect occurs at the corresponding optical energy capture points. In this work, graphene plasmonic time crystals are used to construct transmission waveguides, realizing the modulation of slow light group velocity simply by tuning the chemical potential of graphene. Compared with traditional waveguides such as photonic crystal line defect waveguides[19], its structure is simpler. Even if the structure is fixed, the waveguide performance can be flexibly modulated by changing the applied voltage, which greatly improves the electrical tunability of slow light waveguides. In addition, the SPP wave propagates at the topological boundary as an evanescent wave whose electric field amplitude is continuously attenuated, and the longer the transmission distance, the stronger the attenuation. By applying continuous excitation at the excitation source and recording the field strength superposition process at the optical energy capture point of the waveguide, we intuitively show the electric field change caused by the field strength superposition effect in time, which is not found in the previous slow light research work[11]. Since the modes in the waveguide are not discrete, degeneracy of the forward and backward modes will occur, resulting in energy loss. Therefore, when the optical group velocity is zero in the time sequence, the phenomenon of completely stopping the optical group velocity, the so-called "stationary rainbow", does not actually occur.

4 Conclusion

In this paper, the time crystal band gap is periodically opened and closed by dynamically controlling the periodic change of the external voltage

of the graphene nanodisk with time. Slow light transmission with the group velocity near zero is realized by the slow light waveguide made of graphene plasmon time crystal. The simulation results show that when the light propagates in the waveguide, a group velocity close to zero can be obtained, which is accompanied by the appearance of the field enhancement effect at the corresponding optical energy trapping point of the waveguide. In the case of adjusting the external bias voltage, the operating frequency of the slow optical waveguide can be effectively adjusted. Our research will be applied in the future to devices in the fields of on-chip light buffering and enhanced light-matter interactions.

——中文对照版——

1 引 言

慢光技术在光场调控及光存储器件中的潜在应用前景颇为广阔[1-3], 因而备受关注。通过控制结构色散来实现慢光是目前常用的技术之一, 该技术的主要方法是通过设计特定结构的慢光波导实现对光群速度的控制。已经在多个研究中观察到这类光子晶体波导中产生的慢光[4-5]。然而, 在以往的慢光波导结构中, 当群速度变慢, 其支持的带宽将变得非常狭窄, 同时还伴随着巨大的群速度色散效应。Scheuer J 等人采用结构复杂的耦合谐振光波导实现内部色散补偿, 解决了失真问题[6]。近年来, 人们采用表面等离激元极化子(Surface Plasmon Polaritons, SPPs) 波导来实现慢光, 在结构固定的情况下可以获得更高的慢光容量, 但慢光性能的调整受到限制[7]。同样地, 啁啾结构所具有的极大的群速度色散效应会使光信号严重失真, 并且器件的工作频率范围有限[8]。再者, 传统的慢光器件的结构设计复杂且结构一旦固定其可调谐性能就很差, 从而限制了它们的实际应用。

光子晶体拥有良好的拓扑能带效应, 其拓扑概念在光子学领域的应用中极具潜力, 从而引起了人们的广泛关注。拓扑光子结构已经颠覆了一些关于波传播和操控的传统观点。将拓扑光子晶体应用于波的传播, 可以实现如无反射的急剧弯曲的波、鲁棒的延迟线、自旋极化开关和非互易器件[9], 使新型的光子器件成为可能。最近, 陈晓东等人提出并证明了拓扑光子晶体中的谷态可以作为拓扑保护来实现光的传输, 该设计是将两个拓扑结构不同的拓扑光子晶体镜像放置构成可以实现拓扑保护的界面[10]。之后, Yoshimi 等研究人员提出了一种在谷态光子晶体中实现拓扑慢光波导的结构[11]。该波导结构是基于半导体基底, 实现拓扑带隙范围内群指数大于 100 的慢光传输, 但制作工艺较为复杂, 不具备可调谐性, 同时没有涉及慢光所带来的场强变化。随着研究的深入, 发现在折射率随时间周期性变化的光子时间晶体材料中可以实现谷态这种拓扑带隙结构[12]。方法是通过打破晶体时间平移对称, 光子时间晶体可以实现拓扑非平庸相位[13-15], 从而影响光在晶体中的传播。

众所周知, 石墨烯具有独特的电学和光学特性, 尤其是其支持表面等离子激元波, 具有相对较低的欧姆损耗及较强的可调谐性等优点[16]。Jin 等人设计了具有周期性图案的单层石墨烯, 通过引入静态磁场实现了拓扑单向边界传输[17]。之后, 王洋等学者实现了用于传感应用的双层石墨烯超表面中的拓扑谷等离子体传输[18]。最近, 郭翔等研究人员通过光子晶体线缺陷设计了石墨烯 SPP 等效二维光子晶体慢光波导, 通过石墨烯在空间上的化学势渐变来实现慢光的调制[19]。同样地, 在时间上实现对石墨烯等离激元晶体谷态拓扑慢光传输的调制是非常有意义的工作。本文提出了一种在石墨烯等离激元时间晶体构造的波导中实现拓扑慢光传输的新方法。二维石墨烯等离激元时间晶体由一组呈蜂窝状周期性排列的石墨烯纳米盘组成。通过控制石墨烯的化学势随时间周期性变化, 打破了石墨烯等离激元时间晶体的时间平移对称性。数值仿真表明, 等离激元时间晶体能带带隙可以随时间周期性地打开和闭

合。进一步研究发现：锯齿形边可以支持在拓扑带隙内实现接近零的电磁传输群速度。对慢光波导电磁传输进行数值仿真，模拟结果表明该拓扑波导能够产生慢光。该方法的优点是结构简单，具有较好的场增强效果和动态调谐能力，为动态实现光场调控提供了新的途径和方法。

2 数值仿真方法和模型

本文基于石墨烯等离激元时间晶体实现谷态拓扑慢光传输波导。如图 1(a)(彩图见期刊电子版) 所示，该波导采用 Zigzag 结构拓扑界面作为传输通道，顶部由石墨烯纳米盘构成。石墨烯与空气接触，背景材料选择的是 SiO_2，衬底材料是 Si。从图中的波导截面图可以看出，偏置电压加在石墨烯纳米盘与硅衬底上。其中硅柱按三角晶格排列，$V_1(t)$, $V_2(t)$ 和 $V_3(t)$ 分别是外加在石墨烯纳米盘上的偏置电压，这种方式是基于石墨烯等离激元的光子晶体机理实现的[20]。当石墨烯与衬底之间的距离一定时，通过改变外加电压就可以改变石墨烯的化学势。

假设石墨烯周围环境的相对介电常数分别为 ε_{r1}和ε_{r2}。其中，衬底采用相对介电常数为 ε_{r1}=3.9 的 SiO_2，石墨烯上表面空气的相对介电常数为ε_{r2}=1。在该模型中，数值仿真考虑 TM 模式，假设该 TM 模式的电场形式为[21]：

$$\begin{cases} E_x = A\mathrm{e}^{\mathrm{i}\beta x - Q_1 z},\ E_y = 0, E_z = B\mathrm{e}^{\mathrm{i}qx - Q_1 x},\ (z>0) \\ E_x = A\mathrm{e}^{\mathrm{i}\beta x + Q_2 z},\ E_y = 0, E_z = B\mathrm{e}^{\mathrm{i}qx + Q_2 x},\ (z<0) \end{cases}, \tag{1}$$

将式 (1) 代入麦克斯韦方程组，通过添加石墨烯的表面电导率(σ_g)参与公式变换，并匹配相应的边界条件，得到 TM 模式的色散关系[22]：

$$\frac{\varepsilon_{r1}}{\sqrt{\beta^2 - \dfrac{\varepsilon_{r1}\omega^2}{c^2}}} + \frac{\varepsilon_{r2}}{\sqrt{\beta^2 - \dfrac{\varepsilon_{r2}\omega^2}{c^2}}} = -\frac{\sigma_g i}{\omega\varepsilon_0}, \tag{2}$$

其中ε_0为自由空间中的真空介电常数，ω为等离激元的角频率，c为光在真空的传播速度。在整个计算过程中，只考虑传播常数$\beta \ll \dfrac{\omega}{c}$的情况，因此方程 (2) 简化为以下形式[23]：

$$\beta = \varepsilon_0\left(\frac{\varepsilon_{r1}+\varepsilon_{r2}}{2}\right)\frac{2\omega i}{\sigma_g}, \tag{3}$$

其中β是基于石墨烯 SPP 的传播常数，石墨烯的表面电导率σ_g可随温度 T、化学势μ_c，散射速率τ和角频率ω进行调节，其由带内电子散射σ_{intra}和带间电子跃迁σ_{inter}两个部分组成，根据 Kubo 公式[23]：

$$\sigma_g = \sigma_{\mathrm{intra}} + \sigma_{\mathrm{inter}}, \tag{4}$$

$$\sigma_{\mathrm{intra}} = -\mathrm{j}\frac{\mathrm{e}^2 \mathrm{k_B} T}{\pi\hbar^2(\omega - \mathrm{j}\tau^{-1})}\left[\frac{\mu_c}{\mathrm{k_B}T} + 2\ln(\mathrm{e}^{-\mu_c/\mathrm{k_B}T}+1)\right], \tag{5}$$

$$\sigma_{\mathrm{inter}} = \frac{-\mathrm{j}\mathrm{e}^2}{4\pi\hbar}\ln\left(\frac{2|\mu_c| - (\omega - \mathrm{j}\tau^{-1})\hbar}{2|\mu_c| + (\omega - \mathrm{j}\tau^{-1})\hbar}\right), \tag{6}$$

其中$\mathrm{k_B}$是玻尔兹曼常数，e是电子的电荷，$\hbar$是约化普朗克常数。具体来说，石墨烯的化学势μ_c可以通过外部外加电压有效地调节[20-21, 24-25]。

$$\mu_c(t) = \hbar v_{\mathrm{F}}\sqrt{\frac{\pi C_{ox} V_g(t)}{\mathrm{e}}}, \tag{7}$$

式中v_{F}为费米速度，C_{ox}为栅电容[26]，$V_g(t)$为随时间周期性变化的外加电压。石墨烯纳米盘外加偏置电压随时间周期性变化的曲线，如图 1(b)(彩图见期刊电子版) 所示。通过改变外加在石墨烯纳米盘上的偏置电压 $V_1(t)$, $V_2(t)$ 和 $V_3(t)$，可以改变石墨烯化学势$\mu_{c1}(t)$, $\mu_{c2}(t)$和$\mu_{c3}(t)$。

3 数值仿真结果与讨论

3.1 石墨烯等离激元时间晶体模型及性能

首先，探究了由排列成三角晶格的石墨烯纳米盘阵列组成的二维石墨烯等离激元晶体能带拓扑结构。如图 2(a) 所示，石墨烯等离激元时间晶体结构，虚线区域为晶体元胞，实线部分为晶体的布里渊区，其中$\Gamma - M - K - \Gamma$为简约布里渊区，a 是晶体晶格常数，石墨烯纳米盘半径表示为 r。μ_{c1}, μ_{c2}和μ_{c3}分别是不同石墨烯纳米盘的化学势，由式 (7) 可知，这些石墨烯纳米盘的化学势也是可以随时间作周期性变化的，固可以写成$\mu_{c1}(t)$, $\mu_{c2}(t)$和$\mu_{c3}(t)$[27-29]。通过对石墨烯纳米盘的外加偏置电压加以 $V_1(t)$, $V_2(t)$ 和 $V_3(t)$ 的周期变化，可以在时间上灵活地控制其化学势。在这里，计算了一个周期内若干时刻石墨烯等离激元时间晶体的能带，如图 2(b)(彩图见期刊电子版) 所示。其中，

黑线描绘的是当 t=0 s (即$\Delta\mu_c=\mu_{c1}-\mu_{c2}$=0 eV) 时，石墨烯纳米盘的化学势分别为$\mu_{c1}=\mu_{c2}$=0.3 eV 和$\mu_{c3}$=0.6 eV，两条能带在 K 点处简并相交于狄拉克点，且明显不存在带隙。在化学势随时间周期性变化的过程中，石墨烯等离激元时间晶体的时间平移对称性被打破，狄拉克锥色散将被分裂，带隙将会打开[30]。图 2(b) 中的绿色、蓝色和红色曲线分别描绘了如下 3 个时间节点的能带结构：t_1=1 e^{-12}s (即$\Delta\mu_c$=0.1 eV)，t_2=1.5 e^{-12}s (即$\Delta\mu_c$=0.12 eV) 和 t_3=2 e^{-12}s (即$\Delta\mu_c$=0.14 eV)。很明显，晶体能带带隙随着时间的推移会经历一个从闭合到打开的过程。在这里值得注意的是，这种石墨烯等离激元时间晶体能带随时间的变化是可以在不改变几何结构的情况下进行的。

为了验证石墨烯等离激元时间晶体所具有的特性，本项工作设计了数值仿真实验。如图 3(d) 所示，在一片由石墨烯等离激元时间晶体构成的区域中，将一激励源放置在 P 点处，石墨烯纳米盘的化学势之间的关系$\Delta\mu_c$满足图 3(a) 中的变化规律。在这里，从激发源中激发出频率为 46.50 THz 的电磁波。进一步探究在石墨烯化学势变化的同时，时间晶体能带带隙的变化趋势。通过分析带隙的打开及关闭，当激发波的频率位于导带时，传播现象发生；可当这个频率处在带隙内时，波就不会在这个时间间隔内传播[31-33]。仿真结果如图 3(彩图见期刊电子版) 所示，对传输过程中 4 个时间节点的电场进行截图。随着$\Delta\mu_c$在时间上作周期性变化，分别在t_b=3.20 e^{-12}s，t_c=4.16 e^{-12}s，t_d=5.82 e^{-12}s和t_f=8.24 e^{-12}s 的时序中出现传输和禁止交替现象。而这个结果可以很好地说明，石墨烯等离激元时间晶体通过对化学势进行周期性调控，可以实现能带带隙随时间周期性的打开和关闭。

3.2　Zigzag 拓扑边界结构理论与模型

当石墨烯等离激元时间晶体的时间平移对称性被破坏时，狄拉克锥色散就不会受到保护。从群论的角度来看，当反转对称被打破时 (K 或 K') 点的群对称性会由 C_{3v} 降为 C_3。在能带上的表现为狄拉克锥遭到破坏，原本简并于 K 点的两条能带将被打开[34-35]。能带打开之后，有关能带能谷处的轨道角动量出现变化，通过分析得到了在t_1=1 e^{-12}s (即$\Delta\mu_c$=0.1 eV)，t_2=1.5 e^{-12}s (即$\Delta\mu_c$=0.12 eV) 和t_3=2 e^{-12}s (即$\Delta\mu_c$=0.14 eV) 时刻 K 点的相位分布。如图 4(彩图见期刊电子版) 所示，可以看到在不同时刻两条能带简并在 K 点分别出现了左旋圆极化 (Left-handed Circular Polarized, LCP) 和右旋圆极化 (Right-handed Circular Polarized, RCP) 的相位分布。也就是说，在$\Delta\mu_c$随着时间变化的过程中，时间晶体能带打开后任何时刻下的能谷都拥有方向相反的圆极化轨道角动量。因此，可以通过加载不同轨道角动量的电磁模来构成拓扑边缘的电磁传输，这为利用拓扑边界构造来构建慢光波导提供了理论基础。

研究中采用 Zigzag 拓扑边界来构建慢光波导。这种拓扑结构是由石墨烯等离激元时间晶体构建的，它产生了“时间拓扑边界态”，是拓扑边缘态的时间模拟[13]。打破石墨烯等离激元时间晶体的时间平移对称性会导致能带简并处的狄拉克点被打开，从而形成一个完整的带隙，其中存在拓扑保护边界模式。图 5(a)(彩图见期刊电子版) 中红色虚线所在处为 Zigzag 拓扑界面，通过对黑色虚线内区域采样，在商用仿真软件 COMSOL Multiphysics 中，建立有限周期 (N=19) 的超胞单元模型。部分仿真结果如图 5(a) 的底部所示，可以看出电场分布集中于边界处。本文还计算了不同$\Delta\mu_c$时刻下该边界模的色散关系 (图 5(b)(彩图见期刊电子版))，灰色区域表示投影的体能带图。图 5(b) 还描绘处出了t_1=1 e^{-12}s，t_2=1.5 e^{-12}s 和t_3=2 e^{-12}s 3 个不同$\Delta\mu_c$时刻下的边界态的投影能带[36]。很显然，当$\Delta\mu_c$随时间变化时，在每个时刻上总有与之相应的边界态存在，这就意味着实现了基于石墨烯等离激元时间晶体 Zigzag 拓扑边界态的时间模拟。

3.3　慢光现象和场增强效应

进一步分析上述边界模的色散关系，可以推出在色散曲线的极值点存在群速度为零(慢光)的现象。为了更好地研究存在于该边界态中导模的群速度，将 3 个不同时刻的部分色散曲线绘制于图 6(a)(彩图见期刊电子版) 中，很明显，伴随着严重弯曲的色散，因此导致间隙内慢光模式的存在。根据这些边界模的色散曲线，由角频率ω与群速度v_g关系满足$v_g=\mathrm{d}\omega/\mathrm{d}k$[37-38]，可以计算出群

速度随频率的变化曲线。如图 6(b)(彩图见期刊电子版) 所示，红色曲线是在t_1=1 e^{-12}s 时刻$\Delta\mu_c$=0.1 eV 时的群速度，群速度趋近于零，频率趋于50.2370 THz。当在t_2=1.5 e^{-12}s 时刻，$\Delta\mu_c$=0.12 eV时，电磁波群速度在 50.1149 THz频率处接近于零，以蓝色曲线描绘在图 6(b)中。而在t_3=2 e^{-12}s时刻$\Delta\mu_c$=0.14 eV 时，在频率为 49.9292 THz，群速度接近零，由绿色曲线标出。数值计算结果表明，不同频率的电磁波会在不同时间达到零群速度。也就是说，该拓扑边界可以实现在不同时刻支持某一频率电磁波群速度接近零的慢光。

最后，根据图 1(a) 中所给出的慢光波导模型，在仿真软件 COMSOL 中对其进行二维建模，设计采用 Zigzag 边界结构作为传输通道，激励源位于 *P* 处 (如图 1(a) 所示)。对石墨烯纳米盘的外加偏置电压加以 $V_1(t)$, $V_2(t)$ 和 $V_3(t)$ 的周期变化，可以在时间上灵活地控制其化学势。将一定频率的石墨烯 SPP 波由 *P* 点处发出，可以得到其在波导中随时间传输的整个过程。图 7(彩图见期刊电子版) 给出的是频率分别为 50.2370 THz、50.1147 THz 和 49.9292 THz的平面波在波导中传输的电场强度分布结果。在本次模拟仿真中，取频率为 50.2370 THz 的平面波从t_0=0 s 时刻由 *P* 点处持续性激励，沿波导传输1 e^{-12}s后达到群速度接近零的状态，该 SPP波传输停滞在 *X*=307.998 nm 位置处。图 7(a)(彩图见期刊电子版) 所示是频率为 50.2370 THz 的平面波在t_1=1 e^{-12}s 时刻的电场截图。在平面波群速度接近零后继续保持慢光模式下的持续激励，结果发现 *X*=307.998 nm 位置处 (图 7(a) 中绿点) 的电场强度在 *t*=1.4 e^{-12}s 时刻达到了最大值,且此时的电场强度远大于激励源处的电场强度。将 *t*=1.4 e^{-12}s时刻波导中的电场强度描绘在图 7(b) 中，可以发现此时光能捕获点处的场强 *B* 大于激励源处的场强 *A*。将t_0=0 s 至 *t*=1.4 e^{-12}s 时间段内在绿点位置处电场强度变化过程描绘在图 7(c) 中。可以看到，由于慢光传输中的场增强效应，波导在光能捕获点 (绿点) 处实现了电场强度的持续叠加并高于激励源的增强效果[4]。图 7(d) 展示了频率为 50.1147 THz 的 SPP 波从t_0=0 s 时刻由 *P* 点处持续性激励，沿波导传输时间1.5 e^{-12}s后的电场分布图。SPPs 波传输来到t_2=1.5 e^{-12}s 时刻，在 *X*=667.879 nm 位置处的群速度下降至零。同时还对光能捕获点 *X*=667.879 nm 处 (图 7(d) 中蓝点) 的电场进行了持续观测，得到 *t*=2.98 e^{-12}s时刻的边界处电场分布截面图，如图 7(e) 所示。该结果表明，在 *t*=2.98 e^{-12}s 时刻光能捕获点处的电场强度达到最大值 *D*，并且大于 *P* 点处的电场强度 *C*。图 7(f) 描绘了从时间t_0=0 s 到 *t*=2.98 e^{-12}s，蓝点处的电场强度叠加过程。同理，如图 7(g) 所示，频率为 49.9292 THz 的 SPP 波从t_0=0 s 时刻由 *P* 点处不断的激励，沿波导传输2 e^{-12}s后达到接近零的群速度，波导对于该 SPP 波传输的光能捕获位于 *X*=1029.122 nm 处 (图 7(g) 中红点)。在保持慢光模式下进行持续性激励，观测发现光能捕获处的电场在 *t*=3.22 e^{-12}s 时刻到达最大强度 *F*，该电场强度远大于激励源处的电场强度 *E*，如图 7(j) 所示。从t_0=0 s 至 *t*=3.22 e^{-12}s 时间段内在红点位置处电场强度变化过程描绘在图 7(j)中，同样经历了一个场强叠加的过程。上述模拟仿真过程取了 3 个频率的 SPP 波，分别在改变石墨烯纳米盘外加偏置电压将光群速度调制接近零。在场增强效应的影响下，波导在光能捕获点处实现了电场强度持续叠加并高于激励源处的电场强度。这些结果表明，该慢光波导可以实现不同频率的 SPP 波在不同的时间和位置处停滞下来，并在相应的光能捕获点处发生场增强效应。在这项工作中使用石墨烯等离激元时间晶体构造传输波导，仅通过调谐石墨烯化学势就可以实现对慢光群速度的调制。其与光子晶体线缺陷波导[19] 等传统波导相比，在结构上更为简单，即使结构固定，也可以通过改变外加电压灵活调制波导性能，极大地提高了慢光波导的电可调谐性。此外，SPP 波在该拓扑边界传输表现为电场幅值不断衰减的倏逝波，传输距离愈远衰减愈强。在激励源处施加持续的激励，通过记录波导光能捕获点处的场强叠加过程，在时间上直观地展现了由场强叠加效应所引起的电场变化，是之前对慢光研究工作中所没有的[11]。由于波导中的模式并非是离散的，会发生前后向模式的简并，最终使能量流失。因而在时序中实现光群速度为零时，所谓“静止彩虹”的完全停止光群速度的现象并不会真实发生。

4　结　论

本文通过动态控制石墨烯纳米盘外接电压随时间的周期性变化，使时间晶体的能带带隙周期性地打开和关闭。利用石墨烯等离激元时间晶体制作慢光波导，获得了群速度接近零的慢光传输。仿真结果表明，光在该波导中传播时，可以获得接近零的群速度，并伴随着相应的波导光能捕获点处场增强效应的出现。在调节外部偏置电压的情况下，慢光波导的工作频率可以得到有效的调节。本项研究将在未来应用于片上光缓冲和增强光与物质的相互作用领域的器件中。

References:

[1] JIANG X P, CHEN D B, ZHANG ZH J, *et al*.. Dual-channel optical switch, refractive index sensor and slow light device based on a graphene metasurface[J]. *Optics Express*, 2020, 28(23): 34079-34092.

[2] TORRIJOS-MORÁN L, GRIOL A, GARCÍA-RUPÉREZ J, *et al*.. Slow light bimodal interferometry in one-dimensional photonic crystal waveguides[J]. *Light*:*Science & Applications*, 2021, 10(1): 16.

[3] OSSIANDER M, HUANG Y W, CHEN W T, *et al*.. Slow light nanocoatings for ultrashort pulse compression[J]. *Nature Communications*, 2021, 12(1): 6518.

[4] YAN S Q, ZHU X L, FRANDSEN L H, *et al*.. Slow-light-enhanced energy efficiency for graphene microheaters on silicon photonic crystal waveguides[J]. *Nature Communications*, 2017, 8: 14411.

[5] ZHU K T, DENG T S, SUN Y, *et al*.. Slow light property in ring-shape-hole slotted photonic crystal waveguide[J]. *Optics Communications*, 2013, 290: 87-91.

[6] SCHEUER J. Optimal interfacing with coupled-cavities slow-light waveguides: mimicking periodic structures with a compact device[J]. *Optics Express*, 2017, 25(14): 16260-16273.

[7] CHEN H J. Multiple-Fano-resonance-induced fast and slow light in the hybrid nanomechanical-resonator system[J]. *Physical Review A*, 2021, 104(1): 013708.

[8] NOTOMI M, YAMADA K, SHINYA A, *et al*.. Extremely large group-velocity dispersion of line-defect waveguides in photonic crystal slabs[J]. *Physical Review Letters*, 2001, 87(25): 253902.

[9] ITO H, KUSUNOKI Y, MAEDA J, *et al*.. Wide beam steering by slow-light waveguide gratings and a prism lens[J]. *Optica*, 2020, 7(1): 47-52.

[10] DONG J W, CHEN X D, ZHU H Y, *et al*.. Valley photonic crystals for control of spin and topology[J]. *Nature Materials*, 2017, 16(3): 298-302.

[11] YOSHIMI H, YAMAGUCHI T, OTA Y, *et al*.. Slow light waveguides in topological valley photonic crystals[J]. *Optics Letters*, 2020, 45(9): 2648-2651.

[12] KHANIKAEV A B, SHVETS G. Two-dimensional topological photonics[J]. *Nature Photonics*, 2017, 11(12): 763-773.

[13] LUSTIG E, SHARABI Y, SEGEV M. Topological aspects of photonic time crystals[J]. *Optica*, 2018, 5(11): 1390-1395.

[14] WANG N, ZHANG ZH Q, CHAN C T. Photonic Floquet media with a complex time-periodic permittivity[J]. *Physical Review B*, 2018, 98(8): 085142.

[15] GIERGIEL K, DAUPHIN A, LEWENSTEIN M, *et al*.. Topological time crystals[J]. *New Journal of Physics*, 2019, 21(5): 052003.

[16] GANGARAJ S A H, MONTICONE F. Topological waveguiding near an exceptional point: defect-immune, slow-light, and loss-immune propagation[J]. *Physical Review Letters*, 2018, 121(9): 093901.

[17] JIN D F, CHRISTENSEN T, SOLJAČIĆ M, *et al*.. Infrared topological plasmons in graphene[J]. *Physical Review Letters*, 2017, 118(24): 245301.

[18] WANG Y P, YOU J W, LAN ZH H, *et al*.. Topological valley plasmon transport in bilayer graphene metasurfaces for sensing applications[J]. *Optics Letters*, 2020, 45(11): 3151-3154.

[19] GUO X, WU X, CUI H, *et al*.. Slow light performance enhancement of graphene-based photonic crystal waveguide[J].

Physics Letters A, 2019, 383(16): 1983-1987.

[20] XIONG L, FORSYTHE C, JUNG M, *et al*.. Photonic crystal for graphene plasmons[J]. *Nature Communications*, 2019, 10(1): 4780.

[21] WU X X, YAN M, TIAN J X, *et al*.. Direct observation of valley-polarized topological edge states in designer surface plasmon crystals[J]. *Nature Communications*, 2017, 8(1): 1304.

[22] YOU J W, LAN ZH H, BAO Q L, *et al*.. Valley-Hall topological plasmons in a graphene nanohole plasmonic crystal waveguide[J]. *IEEE Journal of Selected Topics in Quantum Electronics*, 2020, 26(6): 4600308.

[23] 郝影, 孔梅, 卢俊. 带有增益的单微环谐振器的光速控制行为[J]. 中国光学, 2009, 2(6): 482-488.
HAO Y, KONG M, LU J. Control of light speed in single-ring microresonators with gain[J]. *Chinese Optics*, 2009, 2(6): 482-488. (in Chinese)

[24] CAO T, FANG L H, CAO Y, *et al*.. Dynamically reconfigurable topological edge state in phase change photonic crystals[J]. *Science Bulletin*, 2019, 64(12): 814-822.

[25] 洪卫, 王立权, 林嘉平. 高分子多级微相结构与性能的研究进展[J]. 应用化学, 2021, 38(10): 1310-1325.
HONG W, WANG L Q, LIN J P. Research progress of polymeric hierarchical microstructures and their properties[J]. *Chinese Journal of Applied Chemistry*, 2021, 38(10): 1310-1325. (in Chinese)

[26] ZHUANG S N, CHEN J F, LIANG W Y, *et al*.. Zero GVD slow-light originating from a strong coupling of one-way modes in double-channel magneto-optical photonic crystal waveguides[J]. *Optics Express*, 2021, 29(2): 2478-2487.

[27] ZURITA-SÁNCHEZ J R, HALEVI P, CERVANTES-GONZÁLEZ J C. Reflection and transmission of a wave incident on a slab with a time-periodic dielectric function ϵ (*t*)[J]. *Physical Review A*, 2009, 79(5): 053821.

[28] 曹暾, 刘宽, 李阳, 等. 可调谐光学超构材料及其应用[J]. 中国光学, 2021, 14(4): 968-985.
CAO T, LIU K, LI Y, *et al*.. Tunable optical metamaterials and their applications[J]. *Chinese Optics*, 2021, 14(4): 968-985. (in Chinese)

[29] 樊哲, 张盛盛, 唐家豪, 等. 分级纳米材料的结构、制备及其应用[J]. 应用化学, 2020, 37(5): 489-501.
FAN ZH, ZHANG SH SH, TANG J H, *et al*.. Structure, preparation and application of graded nanomaterials[J]. *Chinese Journal of Applied Chemistry*, 2020, 37(5): 489-501. (in Chinese)

[30] MA J, WANG ZH G. Band structure and topological phase transition of photonic time crystals[J]. *Optics Express*, 2019, 27(9): 12914-12922.

[31] SHARABI Y, LUSTIG E, SEGEV M. Disordered photonic time crystals[J]. *Physical Review Letters*, 2021, 126(16): 163902.

[32] CHENG Q Q, PAN Y M, WANG H Q, *et al*.. Observation of anomalous π mode in photonic floquet engingeering[J]. *Physical Review Letters*, 2019, 12: 173901.

[33] ZENG L W, XU J, WANG CH E, *et al*.. Photonic time crystals[J]. *Scientific Reports*, 2017, 7(1): 17165.

[34] PAN Y M, WANG B. Time-crystalline phases and period-doubling oscillations in one-dimensional Floquet topological insulators[J]. *Physical Review Research*, 2020, 2(4): 043239.

[35] 刘慧, 王好南, 谢博阳, 等. 二维光子拓扑绝缘体研究进展[J]. 中国光学, 2021, 14(4): 935-954.
LIU H, WANG H N, XIE B Y, *et al*.. Progress of two-dimensional photonic topological insulators[J]. *Chinese Optics*, 2021, 14(4): 935-954. (in Chinese)

[36] FENG L, ZHU X F,YANG S, *et al*.. Deomonstration of a large-scale optical exceptional point structure[J]. *Optics Express*, 2014, 22(2): 1760.

[37] RAZA S, BOZHEVOLNYI S I. Slow-light plasmonic metamaterial based on dressed-state analog of electromagnetically induced transparency[J]. *Optics Letters*, 2015, 40(18): 4253-4256.

[38] ABOOD I, ELSHAHAT S, OUYANG ZH B. High figure of merit optical buffering in coupled-slot slab photonic crystal waveguide with ionic liquid[J]. *Nanomaterials*, 2020, 10(9): 1742.

Author Biographics:

HE Zhen (1995—), male, from Ganzhou, Jiangxi Province, a master's degree student, received a bachelor's degree in electronic science and technology from Jingdezhen Ceramic Institute in 2018, mainly engaged in the research of photonic crystal materials and optical topological insulators.

何　真(1995—),男,江西赣州人,硕士研究生,2018 年于景德镇陶瓷大学电子科学与技术专业获得学士学位,主要从事光子晶体材料及光学拓扑绝缘体方面的研究。E-mail: hezhen@stu.hqu.edu.cn

QIU Weibin (1971—), male, born in Fujian Province, Ph.D., professor, received his Ph.D. in microelectronics and solid-state electronics and specialty from Institute of Semiconductors, Chinese Academy of Sciences, Beijing in 2003, mainly engaged in the research of semiconductor electronic devices, photonic devices, circuits and systems, supramolecules, topology and topological plasmons.

邱伟彬(1971—),男,福建人,博士,教授,2003 年于北京中国科学院半导体研究所微电子学与固态电子与专业获得博士学位,主要从事半导体电子器件、光子器件、电路与系统、超分子和拓扑等离子体等方面的研究。E-mail: wbqiu@hqu.edu.cn